Halogen-Bonded Hole-Transport Material Suppresses Charge Recombination and Enhances Stability of Perovskite Solar Cells

Laura Canil, Jagadish Salunke, Qiong Wang, Maning Liu, Hans Köbler, Marion Flatken, Luca Gregori, Daniele Meggiolaro, Damiano Ricciarelli, Filippo De Angelis, Martin Stolterfoht, Dieter Neher, Arri Priimagi, Paola Vivo,* and Antonio Abate*

Interfaces play a crucial role in determining perovskite solar cells, (PSCs) performance and stability. It is therefore of great importance to constantly work toward improving their design. This study shows the advantages of using a hole-transport material (HTM) that can anchor to the perovskite surface through halogen bonding (XB). A halo-functional HTM (PFI) is compared to a reference HTM (PF), identical in optoelectronic properties and chemical structure but lacking the ability to form XB. The interaction between PFI and perovskite is supported by simulations and experiments. XB allows the HTM to create an ordered and homogenous layer on the perovskite surface, thus improving the perovskite/HTM interface and its energy level alignment. Thanks to the compact and ordered interface, PFI displays increased resistance to solvent exposure compared to its not-interacting counterpart. Moreover, PFI devices show suppressed nonradiative recombination and reduced hysteresis, with a V_{oc} enhancement of ≥20 mV and a remarkable stability, retaining more than 90% efficiency after 550 h of continuous maximum-power-point tracking. This work highlights the potential that XB can bring to the context of PSCs, paving the way for a new halo-functional design strategy for charge-transport layers, which tackles the challenges of charge transport and interface improvement simultaneously.

1. Introduction

After the ground-breaking work of Miyasaka et al.,[1] the field of perovskite solar cells (PSCs) started to gain worldwide interest. The success of this material is due to its excellent and tunable optoelectronic properties, such as good light absorption coefficient, long carrier diffusion length, and high defect tolerance, combined with easy processing methods.[2–5] Nevertheless, before the wide-scale use of PSCs in real-world applications, several challenges still need to be addressed to improve their performance and especially their stability.[6,7] The best state-of-the-art devices possess complex stoichiometry, which leads to different perovskite surface terminations and the consequent related interactions.[8] For this reason, interfaces play a critical role in the devices' functionality, and their improvement is one of the main challenges that needs to be tackled.[9–12]

L. Canil, Q. Wang, H. Köbler, M. Flatken, A. Abate
Department Novel Materials and Interfaces for Photovoltaic Solar Cells
Helmholtz-Zentrum Berlin für Materialen und Energie
Albert-Einstein-Straße 16, 12489 Berlin, Germany
E-mail: antonio.abate@helmholtz-berlin.de

J. Salunke, M. Liu, A. Priimagi, P. Vivo
Faculty of Engineering and Natural Sciences
Tampere University
P. O. Box 541, Tampere 33014, Finland
E-mail: paola.vivo@tuni.fi

L. Gregori, D. Meggiolaro, D. Ricciarelli, F. De Angelis
Computational Laboratory for Hybrid/Organic Photovoltaics (CLHYO)
Istituto CNR di Scienze e Tecnologie Chimiche "Giulio
Natta" (CNR-SCITEC)
Via Elce di Sotto 8, Perugia 06123, Italy
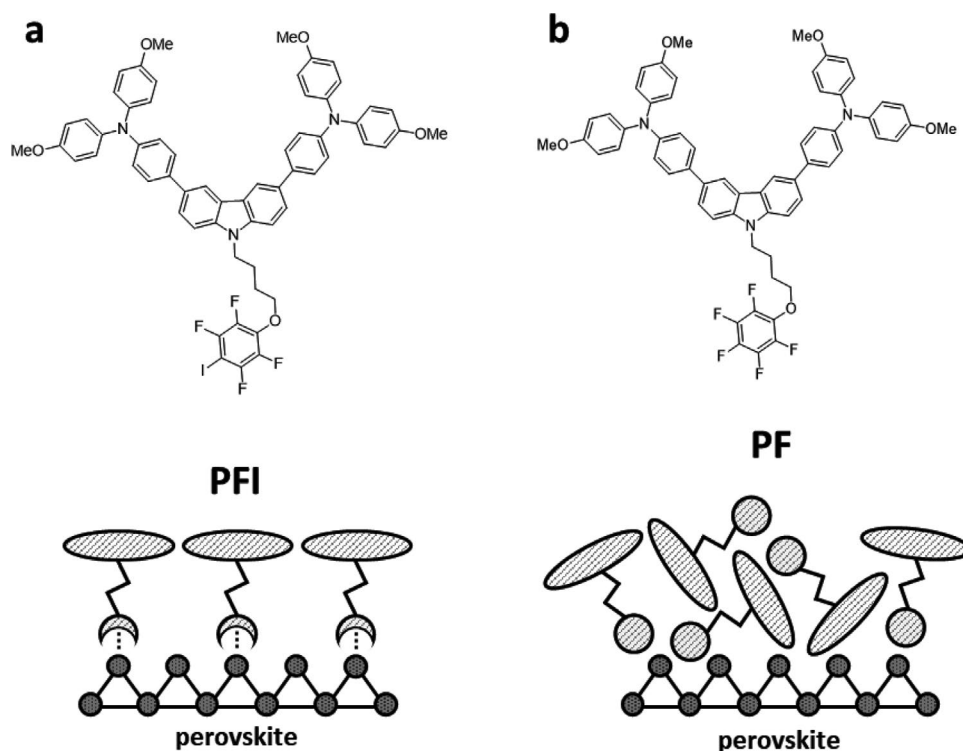
L. Gregori, D. Ricciarelli, F. De Angelis
Department of Chemistry
Biology and Biotechnology
University of Perugia
Via Elce di Sotto 8, Perugia 06123, Italy

F. De Angelis
CompuNet
Istituto Italiano di Tecnologia
Via Morego 30, Genova 16163, Italy

M. Stolterfoht, D. Neher
Institute of Physics and Astronomy
Universität Potsdam
Karl-Liebknecht-Str. 24–25, 14776 Potsdam, Germany

A. Abate
Department of Chemical
Materials and Production Engineering
University of Naples
Federico II, Piazzale Tecchio 80, Naples, Fuorigrotta 80125, Italy

**ADVANCED
SCIENCE NEWS**
www.advancedsciencenews.com

**ADVANCED
ENERGY
MATERIALS**
www.advenergymat.de

Figure 1. Molecular structures and respective hypothesized arrangement on the perovskite surface for a) PFI and b) PF.

One of the most common approaches to optimize interfaces between different layers in PSCs is introducing an interlayer that functionalizes the perovskite surface.[8,13–16] Recently, some works started to integrate this feature in the charge transport layer (CTL) above the perovskite to combine i) interaction with the perovskite surface and ii) charge transport and extraction within one material, thus removing one additional interface.[17–21] All these works have in common the functionalization of perovskite with molecules that bind to the undercoordinated Pb ions. Instead, to our knowledge, no reports exist on exploiting noncovalent interactions between CTLs and the iodide ions on the perovskite surface, of which halogen bonding[22] is a fascinating case.

Halogen bonding (XB) is a non-covalent electrostatically driven interaction between an electrophilic region in a molecule and a nucleophilic region in another, or the same, molecule.[23] The electrophilic region is commonly associated with a polarizable halogen atom substituted in an electron-withdrawing environment. The substitution creates a region of positive electrostatic potential within the molecule called "σ-hole."[24] The σ-hole can interact with electron-rich sites in other molecules, thus forming halogen bonding. XB is of particular interest because of its directionality, tunable interaction strength, and often hydrophobicity.[23,22] Thanks to these unique features, XB has been widely exploited in the context of soft functional materials and crystal engineering,[25] e.g., for the design of supramolecular gels[26] and liquid crystals[27] or the development of light-responsive polymers.[28]

Halogen bonding was first introduced to the PSCs field in 2014 by Abate et al.[29] They functionalized the perovskite surface with iodopentafluorobenzene (IPFB), achieving

suppressed recombination and improved charge extraction due to the screening effect of the molecule on the electrostatic charge of the iodide ions. Later on, various works have highlighted the positive impact of XB on the perovskite crystallographic structure, thus leading to a more symmetric surface.[30–32] Moreover, XB allows the formation of ordered and structured layers, and several studies have reported improved stability and performance in devices.[32–34] Based on these findings, XB appears as an optimal supramolecular strategy to improve interfaces and, consequently, performance and stability in PSCs. However, to the best of our knowledge, there is no report on XB being used in combination with materials with charge-transport properties to obtain CTLs that directly interact with the perovskite surface. Getting such material could enable forming an ordered and neat interface promoting stability and performance in devices without introducing an interlayer between perovskite and CTL.

In this work, we designed a carbazole-based material ($C_{62}H_5F_4IN_3O_5$—named PFI, **Figure 1**a) with good hole selectivity, stability, and energy levels position, which is capable of anchoring to the perovskite surface through XB thanks to a σ-hole generated by the presence of an iodine atom within the molecule.[22,29] We compare the results with PF ($C_{62}H_5F_5N_3O_5$, Figure 1b), a material with the same structure and properties except for the absence of the iodine atom and therefore lacking the ability to form XB. We show that the XB-donating material interacts strongly with the perovskite layer, enhancing the samples' resilience to solvent exposure, improving the energy level alignment in devices and suppressing nonradiative recombination. The employment of PFI as hole-transport material (HTM) in PSCs results in an open-circuit voltage (V_{oc}) enhancement

**ADVANCED
SCIENCE NEWS**

www.advancedsciencenews.com

**ADVANCED
ENERGY
MATERIALS**

www.advenergymat.de

of about 20 mV compared to PF, together with a reduced hysteresis and significantly enhanced stability, maintaining more than 90% of the post burn-in efficiency after 500 h of continuous maximum power point (MPP) tracking and with a projected T_{S80} of ≈2600 h. We ascribe these results to XB between perovskite and the HTM, which allows the formation of an ordered interfacial layer.

We believe that designing materials that can interact with the perovskite surface via specific supramolecular interactions while simultaneously acting as CTLs is crucial for tackling the challenges related to interfaces in PSCs and can bring significant improvement to devices. With this work, we highlight the advantages of XB as the supramolecular interaction of choice in HTM design for PSCs, hoping to pave the way for a new approach to develop tailored charge transport materials for PSCs. In our opinion, combining the advantages of halofunctional HTMs with other approaches, such as dopant-free materials, will ultimately lead to highly efficient and stable perovskite devices.

2. Results and Discussion

PFI and PF were prepared through simple synthetic methods described in detail in the Supporting Information and characterized via ^{1}H and ^{13}C NMR and high-resolution mass spectroscopy (Figures S2–S5, Supporting Information). As a result, the production cost of these materials is around 30 \$ g^{-1} for both PFI and PF (see detailed costs and calculations in Table S1, Supporting Information), much cheaper than for widely reported HTMs such as spiro-OMeTAD (raw material cost is 91.67 \$ g^{-1}[35]).

Figure 1 shows the molecular structure of the two materials and the respective expected arrangement on the perovskite surface. As mentioned above, the presence of σ-hole in PFI allows the material to form XB with the halides on the perovskite. At the same time, the pentafluoro moiety in PF is unable to interact via XB and does not form specific chemical interactions. Therefore, PF can act as a reference to explore the effects of PFI's XB with perovskite.

We can think of these materials as a composition of two parts serving distinct functions: the carbazole-based core, responsible for the energy levels and hole-transport properties, and the fluorinated ring, connected to the core through an alkyl chain, responsible for interactions with the perovskite surface. As represented in Figure 1a, we can simplistically depict PFI as an HTM with a clawed arm, which allows the material to anchor to the surface via XB and form an ordered layer. On the contrary, PF molecules will most likely assume a random distribution on the perovskite, as schematized in Figure 1b. We hypothesize that the improved interface with PFI can promote stability and prevent ion accumulation, thereby bringing several advantages to the devices.

The moiety which is responsible for XB in PFI was already proven to form such bond with perovskite by Abate et al.[29] and later further investigated by Zhang et al.[30] However, we performed additional theoretical and experimental analyses to understand the interaction of the molecules with the surface and to find evidence of the anchoring properties of PFI.

First, we simulated the interaction of PFI and PF with MAPbI$_3$ surface, considered as the prototype lead halide perovskite. The adsorption of the molecules has been modeled on the (001) surface of tetragonal MAPbI$_3$ in the supercell approach for MAI-terminated and PbI$_2$-terminated surfaces,[36–38] where MAI is methylammonium iodide. The computational details are reported in the Supporting Information.

The simulations reveal that, irrespective of the molecule-slab orientation and the termination of the perovskite surface, PFI consistently exhibits adsorption energy two to three times higher than that for PF, evidence of a much stronger interaction of the former with the perovskite surface. Although the adsorption of PFI is favored in a parallel adsorption mode, i.e., with the phenyl ring placed parallel to the perovskite surface (see Figure S10, Supporting Information), the I···I$^-$ interaction is instead maximized when the molecule is placed in perpendicular configuration (see **Figure 2**a), showing an almost linear interaction angle. This trend is expected from the directional nature of XB due to the narrow positive area corresponding to the σ-hole.[22] In contrast, the low adsorption energy of PF suggests that there is no preferred interaction for this molecule, and its distribution and orientation probably depends on weak intermolecular interactions within adsorbed molecules. Our simulations thus suggest the presence of XB between PFI and the perovskite layer. Moreover, the strength of the PFI–perovskite interaction compared to the PF–perovskite interaction supports our interpretation that PFI can anchor itself to the perovskite, likely providing a well-defined layer at the interface. In contrast, PF molecules will probably assume random orientations and, therefore, a less uniform and compact distribution. These results are coherent with the first-principles analysis performed by Zhang et al.[30] on the adsorption of IPFB, which correspond to the part of PFI capable of interaction. In that study, the authors show that IPFB adsorption positively affects the structure and orientation of perovskite at the interface. The molecule resides stably at its position on the surface, with adsorption energy comparable to that calculated for PFI.

Experimental evidence that PFI, in contrast to PF, interacts with the perovskite surface is given in Figure 2b. Here, we used Kelvin Probe (KP) to measure the work function (WF) of doped PFI and PF spin-coated with different concentrations on the perovskite layer. We used the so-called triple-cation perovskite with precursor solution composition Cs$_{0.05}$(MA$_{0.15}$FA$_{0.85}$)$_{0.95}$Pb(I$_{0.85}$Br$_{0.15}$)$_3$. Since the measurements were performed in air, we also determined the WF of perovskite/spiro-OMeTAD samples and used it as a reference instead of bare perovskite, whose WF would be strongly affected by air exposure. The results show that for PFI, the WF increases with the solution concentration. The increase in WF is coherent with the energetics change induced by the intrinsic dipole of the molecule.[39,40] Moreover, upon XB, a partial negative charge moves from the perovskite surface to the molecule,[30,41] leaving the surface slightly more positive than the molecule and therefore forming an additional interfacial dipole pointing toward the surface as well. The dependence of the WF from the solution concentration is an indication that PFI progressively anchors to the ions on the surface until the formation of a uniform layer, and the more molecules are present in the solution (and consequently bind to the perovskite), the more the WF is
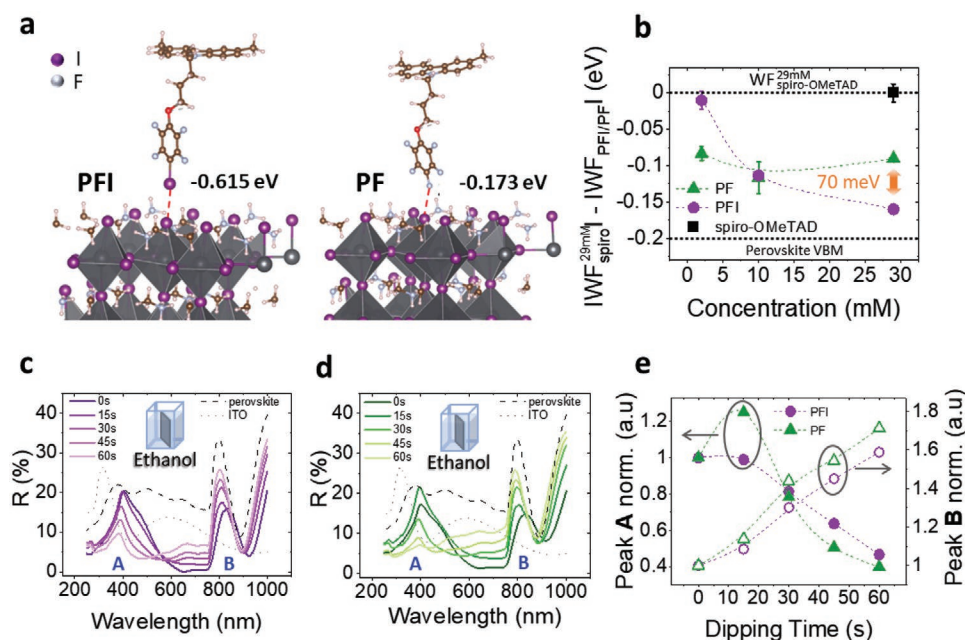
Figure 2. a) Density functional theory simulations of the adsorption of PFI (left) and PF (right) on MAPbI$_3$ perovskite exemplified for the case of MAI-terminated surface with an indication of the respective adsorption energies (Pb-terminated surface in SI). b) KP measurements showing how the WF of PFI and PF changes for different solution concentrations and compared to the WF of doped spiro-OMeTAD at 29 mM (i.e., the concentration used for all HTMs in devices). The WF of spiro-OMeTAD at 29 mM is determined experimentally, while the typical position of the perovskite VBM is shown as reference for the energy level alignment. Measurements performed in air on fluorine-doped tin oxide (FTO)/TiO$_2$/perovskite/HTM samples. c,d) UV-vis reflection spectra of c) ITO/perovskite/PFI and d) ITO/perovskite/PF samples after immersion in ethanol for different time intervals. e) Comparison of the change in intensity of the peak at A and B from (c) and (d) depending on the dipping time.

increased.[38] Therefore, the behavior of PFI corroborates the idea that the molecule interacts with ions on the perovskite surface. On the other hand, the results show that the WF of PF remains constant, although still higher than that of spiro-OMeTAD. This suggests that the PF does not bind to anything specific. The molecules distribute randomly on the perovskite surface, thus creating an initial WF shift that does not change if the concentration of the molecules is varied.

These measurements bring evidence of the interaction of PFI with the perovskite and highlight the effects of the XB capability of PFI on the energy level alignment. In Figure 2b, we show the approximate position of the perovskite valence band maximum (VBM) compared to the spiro-OMeTAD WF (which, in the case of doped HTMs, is close to the highest occupied molecular orbital (HOMO) position[42]). The position of the VBM was chosen so that the offset with spiro-OMeTAD is 200 mV, as reported in the literature for the exemplary case of MAPbI$_3$.[43] We can see that, at the concentration used in devices (i.e., 29×10^{-3} M), the offset between perovskite VBM and PFI HOMO level is reduced compared to that with PF, improving the energy level alignment. A more explicit representation of the energy level alignment is reported in Figure S19 in the Supporting Information. These results are even more interesting considering that, if we look at the single molecules, PF has a slightly stronger dipole than PFI (Table S5, Supporting Information), and thus it should, in principle, have a higher WF. Therefore, the higher WF measured for PFI is related to the material's capability of binding to the halide ions through XB. Indeed, this favors the formation of a compact and ordered

layer where the dipoles point mainly in the same direction, leading to a more significant collective energetic shift[40] compared to PF, which assumes a more irregular distribution the dipoles likely pointing toward random directions.

To further demonstrate the presence of an interaction between PFI and perovskite, we prepared perovskite/HTMs samples and tested their resilience to solvent exposure. The samples were immersed for 15 s in ethanol (a solvent that can slowly dissolve the materials) and, immediately after, UV-vis absorption spectra were recorded to assess any possible change in the films, which can be detected through changes in the optical properties. The measurements were done in reflection mode to be more surface sensitive and focus on the HTM layers rather than the perovskite bulk. The procedure was repeated several times up to 60 s of solvent exposure to monitor the dissolution process of PFI and PF.

Figure 2c,d shows how the reflection spectra for PFI and PF change for different dipping time intervals. The peaks at ≈400 nm (A in Figure 2) are characteristic of the two HTMs (see UV-vis of the pure materials in Figure S6, Supporting Information), while the peaks at ≈800 nm (B in Figure 2) are associated with the perovskite layer detected through the HTMs. As a reference, the figures also show the signals for the indium tin oxide (ITO) substrate and the bare perovskite layer. With this in mind, we can compare the two materials and observe as a general trend that A decreases with dipping time while B increases. This means that the signal coming from the HTMs is decreasing in intensity with dipping time, while that related to the perovskite is increasing, which matches the idea

Table 1. Optoelectronic properties of PFI, PF, and spiro-OMeTAD. λ_{abs} is the absorption wavelength, E_g is the bandgap, μ is the hole mobility. Energy levels measured in solution and without dopants. Measurements details in Supporting Information.

HTM	λ_{abs} [nm]		HOMO [eV]	LUMO [eV]	E_g [eV]	μ [cm^2 V^{-1} s^{-1}]	
	Liquid[a]	Solid				Undoped	Doped
PFI	336	337	4.96	1.86	3.1	2.0×10^{-5}	2.2×10^{-4}
PF	336	337	4.97	1.87	3.1	2.5×10^{-5}	2.0×10^{-4}
Spiro-OMeTAD			4.82			6.0×10^{-5}	7.2×10^{-4}

[a]Measured in chlorobenzene solution (10^{-5} м).

that the two materials are dissolving and "exposing" more the underneath layer, i.e., the perovskite. Figure 2e highlights the behavior of the two materials by showing A and B normalized at the initial condition, i.e., before exposure to ethanol. The results after the first 15 s in ethanol are particularly interesting. We can observe how for PFI, the intensity of the A peak remains stable, while for PF, we can see an increase in the signal. We interpret the latter as due to the formation of agglomerates of PF at the surface, indicating easy desorption of PF in ethanol. After exposing the sample to the solvent for a further 15 s, the signal decreases to under the initial value and keeps this trend for the following dipping sessions. Therefore, it seems that PF clusters are initially formed due to the material desorption and are afterward washed away while the film is slowly dissolving.

On the other hand, the fact that PFI remains stable during the first 15 s of solvent exposure indicates that the material is more resilient to dissolution. This can be ascribed to XB between PFI and the halide ions at the perovskite surface, which makes more difficult to detach molecules and increases the hydrophobicity of PFI thanks to the formation of a more ordered layer, making it more resistant to polar solvents. The increase in hydrophobicity is furthermore supported by water contact angle measurements, showing a contact angle of more than 92° in the case of PFI and 89° for PF (Figure S7, Supporting Information).

It is also relevant to note that, after the initial 15 s of ethanol dipping, the A peak for PF starts to decrease at a faster rate than for PFI, indeed indicating a different resistance to re-solubility for the two materials. Similar observations can be done for the evolution of peak B: the stronger it becomes, the more we "see" the perovskite layer, i.e., the thinner the HTM. As highlighted in Figure 2e, the B peak for PF increases its intensity faster than PFI, especially during the first 30 s.

To further support the results, we repeated the test while measuring UV-vis in transmission mode (Figure S12, Supporting Information). In this case, since most of the signal comes from the perovskite layer, it is more difficult to draw conclusions. Nevertheless, we could notice that, except for an initial shift after the first dipping interval, the PFI spectrum remains almost unchanged, while the PF one becomes more and more similar to the perovskite reference, indicating likely an increased dissolution of the material.

As complementary measurement to UV-vis and to strengthen our claim, we additionally recorded images via atomic force microscopy (AFM). We exposed the PFI/PF-coated films to the solvent and monitored the change in topography. The results are reported in Figure S13 in the Supporting Information and

are coherent with the trend observed through UV-vis. Specifically, we observe that upon solvent exposure holes start to form on the surfaces and their density increases after every treatment. However, while PF displays a high density of holes directly after the first exposure to ethanol, PF seems to remain more stable, with the formation of agglomerates, but not evident damage. Overall, it appears that PF degrades faster than PFI upon ethanol treatment.

Together with allowing us to further monitor the dissolution process, AFM images of two different untreated PFI and PF films (Figure S14, Supporting Information) showed features that could be evidence of diverse stacking for the two materials. In particular, PF presents some imperfections displaying holes in a circular pattern, which are instead absent in PFI films. This might suggest that the ordered interfacial monolayer formed in the case of the halogen-bonded PFI molecules can help the growth of more compact and uniform upper layers compared to PF. Therefore, we speculate that the patterns of holes visible for the latter could be related to a less compact stacking.

Overall, the findings from UV-vis and AFM support the beneficial effects of XB and clearly show how the capability of an HTM of interacting with the underneath layer, in our case perovskite, can positively affect its hydrophobicity and resilience to dissolution, resulting in improved stability of the whole system.

Until now, we showed how PFI could anchor to the halides on the perovskite surface through XB, promoting the formation of an ordered and stable interfacial layer compared to the reference PF. To evaluate the applicability of these materials in devices and assess the related effects, we tested their optical properties, energy levels, and hole mobility. The relevant results are highlighted in **Table 1**, while further details are reported in the Supporting Information. UV-vis absorption measurements in liquid and solid-state show negligible absorbance in the visible range, thus excluding an interference between HTMs and perovskite absorption. The energy levels of undoped materials reported in Table 1 were determined through differential pulse voltammetry, while the WF of the doped HTMs were compared with that of spiro-OMeTAD through KP measurements (as previously discussed and shown in Figure 2b).

Moreover, we measured the mobilities through the space-charge-limited-current method,[44] both with and without dopants. The two materials exhibit comparable values, just slightly lower than those measured for spiro-OMeTAD as reference. These results suggest that the HTMs are suitable for perovskite-based devices.

Hence, we prepared *n-i-p* devices with doped PFI and PF as hole transport layers and tested the respective performances.
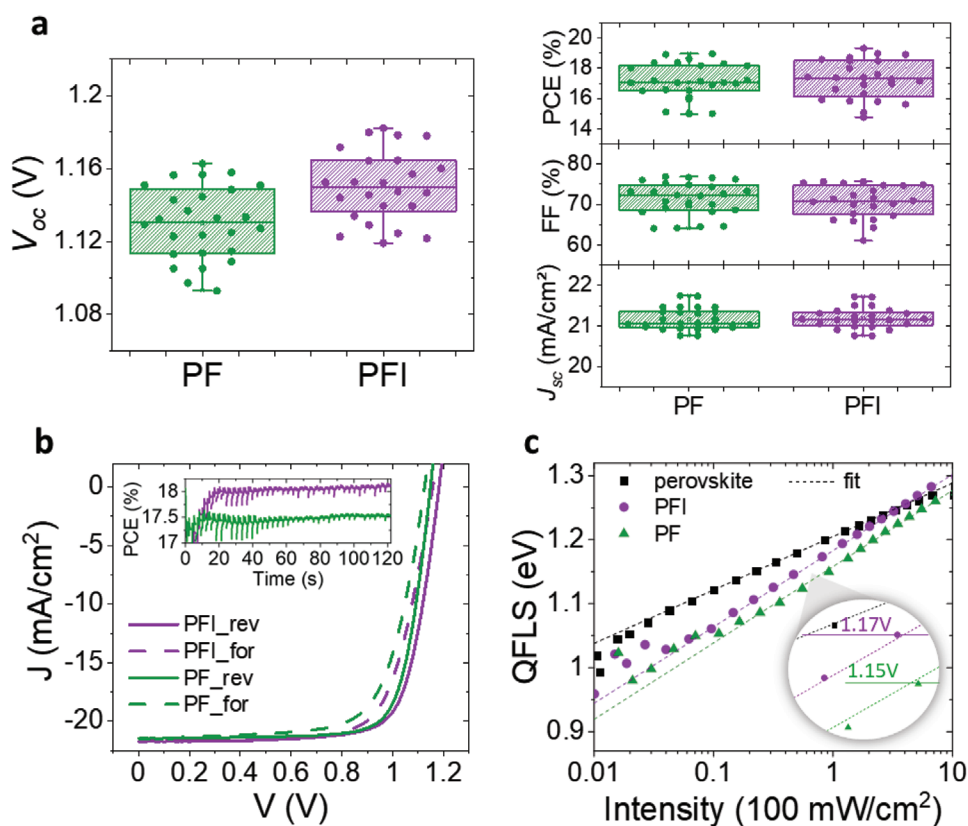
Figure 3. a) Photovoltaic parameters of *n-i-p* devices with structure FTO/TiO$_2$/perovskite/HTMs/Au, box charts from 12 and 13 pixels (i.e., single solar cells) for PFI and PF, respectively, reverse and forward scans. b) *J–V* curves of the best pixels recorded at 100 mV s^{-1} scanning speed in the inset MPP-tracking of the reported pixels. c) Absolute steady-state PL measurements for different light intensities showing the QFLS for glass/perovskite and glass/perovskite/HTMs (doped), with a highlight on the difference in values between PF and PFI. Measurements performed on the film side.

Statistics on the resulting photovoltaic parameters are reported in **Figure 3**a and **Table 2**, together with the values for the best pixels. Furthermore, in Table 2, we also report the results for devices with spiro-OMeTAD as HTM (fabricated in identical conditions) to highlight that PFI- and PF-based solar cells can reach the same efficiency as those with the state-of-art HTM spiro-OMeTAD. It is worth noting that we chose spiro-OMeTAD as reference because of its wide use, however other HTMs enabled reaching high efficiency, sometimes even without the use of dopants.[45–50] We believe our own concept of halo-functional HTM could be further developed to achieve even higher efficiencies, ideally without the need of doping. Therefore, with this work we wish to show the advantages of this kind of HTM and we hope to pave the way to a new set of halo-functional materials leading to high efficiency and stable devices.

The results reported in Figure 3 show that employing PFI over PF as HTM has positive effects on devices, especially in terms of reduction of interfacial charge recombination and ion density. As reported in the literature, the XB functionalization does not change the optoelectronic properties of the substrates;[32,33] therefore, it is essential to point out that its advantages instead come from the ordered and homogenous distribution of the molecules at the interface. FF and J_{sc} remain similar in the two cases, while there is a definite V_{oc} improvement in devices comprising PFI, leading to an increase in power conversion efficiency (PCE), especially visible from the stabilized power output in the inset in Figure 3b. Specifically, we observe an average V_{oc} enhancement of about 20 mV, increased to more than 30 mV for the best pixels, which suggests that PFI suppresses the charges' capability of recombining

Table 2. Photovoltaic parameters and hysteresis index (H-index) of devices with PFI, PF, and spiro-OMeTAD for the best pixels and the average (avg.) of 12, 13, and 14 pixels, respectively. The stabilized power output corresponding to the best pixels for 120 s MPP-tracking is also reported. H-index is calculated as PCE$_{rev}$/PCE$_{for}$, where rev and for are reverse and forward scan, respectively.

HTM	PCE [%]			V_{oc} [mV]		FF [%]		J_{sc} [mA cm^{-2}]		H-index	
	Best$_{JV}$	Best$_{stabilized}$	Avg.	Best	Avg.	Best	Avg.	Best	Avg.	Best	Avg.
PFI	19.3	18.1	17.3	1182	1150	75	72	21.7	21.3	1.08	1.07
PF	19.0	17.5	17.1	1148	1130	77	71	21.5	21.2	1.18	1.12
Spiro-OMeTAD	19.5	19.3	18.0	1181	1154	75	72	22.2	21.0	1.05	1.07
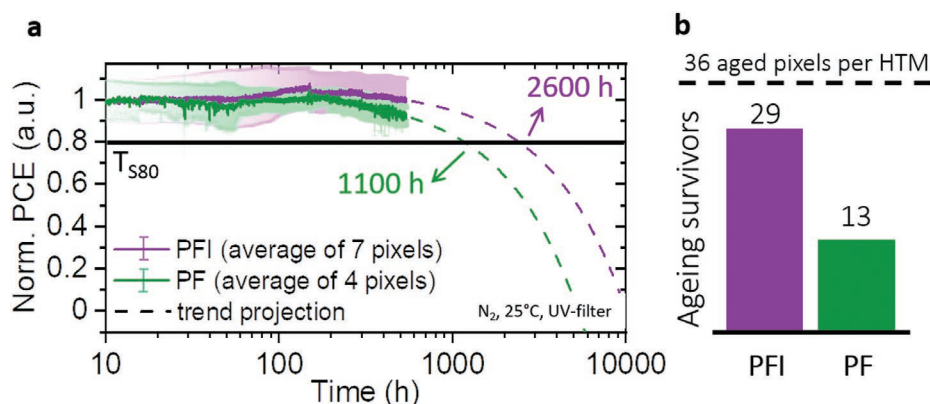
Figure 4. a) Normalized PCE of FTO/TiO$_2$/perovskite/HTMs/Au devices for ≈550 h of continuous MPP-tracking under 1 sun illumination. The measurements were performed through a custom-made ageing setup in an N$_2$ atmosphere with a UV-blocking filter. The device temperature was actively kept at 25 °C. Average of 7 pixels for PFI and 4 pixels for PF corresponding to one measured batch. Another batch was tested, leading to the same trends (Figure S23, Supporting Information). Pixels showing significantly different performances were removed from the average. Data are plotted in log scale, with error bars (standard deviation) and were normalized to the value at 10 h, corresponding to the end of the so-called "burn-in."[58] Dashed lines represent the linear projection of the stability trend to identify the time at which 80% of the efficiency from the end of burn-in is reached (T_{S80}[59]). b) Statistics displaying the pixels that still showed power output after the test and did not show any unusual behavior during the test ("ageing survivors") compared to the total number of aged pixels in the course of two tests. A pixel is a single solar cell in a device.

at the perovskite/HTM interface. This behavior is confirmed by the data shown in Figure 3c. We measured PL on perovskite/HTM stacks, with doped HTMs, and the neat perovskite layer at different light intensities to extract the internal voltage of the partial cell stack, i.e., the quasi-fermi level splitting (QFLS). Considering that the QFLS of the perovskite/HTM stack is almost identical to the neat layer at one sun, this measurement highlights that PFI nearly overcomes the interfacial recombination loss typically caused by the deposition of an HTM on top of perovskite. This scenario is particularly relevant since it is one of the leading causes of V_{oc} loss in PSCs.[11,51,52] Moreover, the difference between the QFLS of PFI and PF at one sun is around 20 mV, matching perfectly with the V_{oc} enhancement obtained from the devices. This measurement, therefore, highlights the ability of PFI to suppress recombination and confirms that the increase in V_{oc} is related to the difference between PFI and PF, i.e., the ability of PFI of forming XB and thus a neat interface. In particular, we ascribe this result to the improved energy level alignment previously discussed (Figure 2b). Indeed, PFI and PF as isolated molecules have the same HOMO level position (see Table 1), but once deposited on perovskite, their dipoles comes into play affecting the interfacial energetics. Thanks to XB, PFI can assemble on the perovskite surface, forming a uniform and compact layer and generating a bigger collective dipole. By looking at Figure 2b, we can see that this leads to a difference of around 70 meV between the WF of PFI and PF at the conditions employed in the devices (29 mM). As a result, the offset between PFI HOMO level and perovskite valence band is smaller than that for PF, obtaining a more favorable energy level alignment and a consequent V_{oc} improvement (Figure S19, Supporting Information).

The positive effect of PFI in suppressing the recombination is also supported by a reduction of the hysteresis in the J–V curves, as evident in Figure 3b and stressed by the hysteresis indexes (H-indexes) calculated in Table 2. It is indeed known from the literature that hysteresis mainly arises from the absorber material and that interfaces and CTLs are

fundamental for its reduction.[53,54] Specifically, hysteresis is often correlated with the detrimental effect of mobile ions[55–57] and, in our case, PFI is likely to limit their migration by anchoring itself to the under-coordinated halide ions on the perovskite, promoting the formation of a better-terminated surface compared to PF. Additionally, we observed an increase in shunt resistance for devices with PFI (Figure S17, Supporting Information), a sign of reduced defects density.

The advantages of using a halo-functional HTM in perovskite-based devices are evident in the photovoltaic performance of the devices and their stability under working conditions. Using a custom-made ageing setup, we performed identical ageing tests according to ISOS-L-1I[59] on two different batches of devices. All pixels were tested in a controlled environment under continuous MPP-tracking at one sun illumination to assess their long-term stability. In **Figure 4**a, we report the results of one of the tests as an example, while the other one is shown in Figure S23 in the Supporting Information. In the case presented in Figure 4a, the devices were aged for ≈550 h, and the displayed MPP tracks are the average of 7 pixels and 4 pixels for PFI- and PF-based devices, respectively. Pixels showing significantly different performances were removed from the average. The data were normalized to the value at ≈10 h, after the so-called "burn-in,"[58] and plotted in logarithmic scale from that point with error bars giving the standard deviation. A plot in linear scale and from 0 h is displayed in Figure S22 in the Supporting Information. Both PF- and PFI-based devices retain more than 90% of their initial efficiency during the measurement, evidence of excellent stability. Devices with PFI as HTM show enhanced stability compared to devices with PF. Although the difference is not large, it is significant considering that the trends represent the averages of several devices. This result is of particular importance because, in real-world applications, a long-term stable energy output is more relevant than the efficiency obtained from J–V curves. As an approximation, we projected their stability trend linearly to identify the probable T_{S80},[58,59] i.e., the time at which the efficiency has reached

**ADVANCED
SCIENCE NEWS**

www.advancedsciencenews.com

**ADVANCED
ENERGY
MATERIALS**

www.advenergymat.de

80% of the value after burn-in. We can observe that PFI-based devices deliver a remarkable projected T_{S80} of ≈2600 h, more than double of that extrapolated for PF-based devices.

It is also significant to note that the number of devices which remained operational after the ageing test is higher for PFI. Indeed, as represented in Figure 4b, if all the tested devices (six devices per HTM with a total of 36 pixels per HTM) are taken into account, less than half of the pixels using PF as HTM survived the ageing test, in contrast to devices with PFI which show a more than 80% of working pixels. Note that our statistics count as "non-operational" devices that do not show power output after the test and devices that displayed particularly unusual behaviors during the test.

PSCs' operational stability can be affected by different external and internal elements.[60] Considering that our ageing tests were performed in an N_2 atmosphere and at controlled temperature, the observed difference in stability is likely connected to intrinsic factors. In particular, as already mentioned before, the ability of PFI to anchor to the halide ions on the perovskite can prevent them from moving under light and bias. It is believed that ion migration is one of the primary sources for PCSs' intrinsic degradation.[61,62] Indeed this phenomenon leads to vacancies and other defects, therefore increasing the number of recombination centers. Moreover, ions can accumulate at interfaces and create unfavorable electric fields. For these reasons, the interaction between PFI and the I^- ions likely plays an essential role in limiting ion migration, reducing hysteresis, and improving the long-term operational stability of the devices, which is a result of high importance considering that stability is one of the main problems associated with PSCs.

3. Conclusions

In conclusion, we have designed and developed a halo-functional material (PFI) that can both act as HTM and anchor to the perovskite surface through halogen bonding, forming a well-ordered interface. We compared the results for PFI with a reference material (PF) identical in structure except for the iodine atom enabling the interaction. Theoretical and experimental evidence suggests that PFI has a strong and directional interaction with the perovskite surface that makes the samples more resilient to degradation than PF and improves the energy level alignment at the perovskite/HTM interface. Moreover, the presence of halogen bonding leads to suppression of recombination and ion migration. This is reflected in a ≥20 mV V_{oc} improvement, reduction in the J–V hysteresis and operational stability enhancement in the corresponding devices. Solar cells with PFI as HTM display excellent stability after 550 h under continuous MPP-tracking and with a projected T_{S80} of ≈2600 h, which is more than double than what was obtained for devices with PF. These results display the benefits of halogen bonding and prove it to be a successful concept in the context of PSCs. By combining charge transport capability and the ability to interact with the iodides on the perovskite surface into one material, we created an HTM that can orderly anchor to the perovskite layer, thus promoting a well-defined interface, which is critical for obtaining efficient and, most importantly, stable PSCs.

Supporting Information

Supporting Information is available from the Wiley Online Library or from the author.

Conflict of Interest

The authors declare no conflict of interest.

Data Availability Statement

Data are available on request from the authors.

[1] A. Kojima, K. Teshima, Y. Shirai, T. Miyasaka, *J. Am. Chem. Soc.* **2009**, *131*, 6050.

[2] J. P. Correa-Baena, A. Abate, M. Saliba, W. Tress, T. Jesper Jacobsson, M. Grätzel, A. Hagfeldt, *Energy Environ. Sci.* **2017**, *10*, 710.

[3] J. S. Manser, J. A. Christians, P. V. Kamat, *Chem. Rev.* **2016**, *116*, 12956.

[4] A. K. Jena, A. Kulkarni, T. Miyasaka, *Chem. Rev.* **2019**, *119*, 3036.

[5] M. A. Green, A. Ho-Baillie, *ACS Energy Lett.* **2017**, *2*, 822.

[6] N. G. Park, M. Grätzel, T. Miyasaka, K. Zhu, K. Emery, *Nat. Energy* **2016**, *1*, 16152.

[7] J.-P. Correa-Baena, M. Saliba, T. Buonassisi, M. Grätzel, A. Abate, W. Tress, A. Hagfeldt, *Science* **2017**, *358*, 739.

[8] B. Chen, P. N. Rudd, S. Yang, Y. Yuan, J. Huang, *Chem. Soc. Rev.* **2019**, *48*, 3842.

[9] P. Schulz, D. Cahen, A. Kahn, *Chem. Rev.* **2019**, *119*, 3349.

[10] M. Lira-Cantú, *Nat. Energy* **2017**, *2*, 17115.

[11] C. M. Wolff, P. Caprioglio, M. Stolterfoht, D. Neher, *Adv. Mater.* **2019**, *31*, 1902762.

[12] L. K. Ono, Y. Qi, *J. Phys. Chem. Lett.* **2016**, *7*, 4764.

[13] H. Zhang, M. K. Nazeeruddin, W. C. H. Choy, *Adv. Mater.* **2019**, *31*, 1805702.

[14] Y. Shao, Z. Xiao, C. Bi, Y. Yuan, J. Huang, *Nat. Commun.* **2014**, *5*, 5784.

[15] T. H. Han, S. Tan, J. Xue, L. Meng, J. W. Lee, Y. Yang, *Adv. Mater.* **2019**, *31*, 1803515.

[16] J. Peng, J. I. Khan, W. Liu, E. Ugur, T. Duong, Y. Wu, H. Shen, K. Wang, H. Dang, E. Aydin, X. Yang, Y. Wan, K. J. Weber, K. R. Catchpole, F. Laquai, S. De Wolf, T. P. White, *Adv. Energy Mater.* **2018**, *8*, 1801208.

[17] X. Ding, H. Wang, C. Chen, H. Li, Y. Tian, Q. Li, C. Wu, L. Ding, X. Yang, M. Cheng, *Chem. Eng. J.* **2020**, *410*, 128328.

[18] B. X. Zhao, C. Yao, K. Gu, T. Liu, Y. Xia, Y.-L. Loo, *Energy Environ. Sci.* **2020**, *13*, 4334.

[19] S. Y. Wang, C. P. Chen, C. L. Chung, C. W. Hsu, H. L. Hsu, T. H. Wu, J. Y. Zhuang, C. J. Chang, H. M. Chen, Y. J. Chang, *ACS Appl. Mater. Interfaces* **2019**, *11*, 40050.

[20] F. Qi, X. Deng, X. Wu, L. Huo, Y. Xiao, X. Lu, Z. Zhu, A. K. Y. Jen, *Adv. Energy Mater.* **2019**, *9*, 1902600.

[21] J. Zhang, S. Guo, M. Zhu, C. Li, J. Chen, L. Liu, S. Xiang, Z. Zhang, *Chem. Eng. J.* **2021**, *408*, 127328.

[22] G. Cavallo, P. Metrangolo, R. Milani, T. Pilati, A. Priimagi, G. Resnati, G. Terraneo, *Chem. Rev.* **2016**, *116*, 2478.

[23] G. R. Desiraju, P. S. Ho, L. Kloo, A. C. Legon, R. Marquardt, P. Metrangolo, P. Politzer, G. Resnati, K. Rissanen, *Pure appl. Chem.* **2013**, *85*, 1711.

[24] T. Clark, M. Hennemann, J. S. Murray, P. Politzer, *J. Mol. Model.* **2007**, *13*, 291.

[25] A. Mukherjee, S. Tothadi, G. R. Desiraju, *Acc. Chem. Res.* **2014**, *47*, 2514.

[26] L. Meazza, J. A. Foster, K. Fucke, P. Metrangolo, G. Resnati, J. W. Steed, *Nat. Chem.* **2013**, *5*, 42.

[27] H. Wang, H. K. Bisoyi, A. M. Urbas, T. J. Bunning, Q. Li, *Chem. – Eur. J.* **2019**, *25*, 1369.

[28] M. Saccone, V. Dichiarante, A. Forni, A. Goulet-Hanssens, G. Cavallo, J. Vapaavuori, G. Terraneo, C. J. Barrett, G. Resnati, P. Metrangolo, A. Priimagi, *J. Mater. Chem. C* **2015**, *3*, 759.

[29] A. Abate, M. Saliba, D. J. Hollman, S. D. Stranks, K. Wojciechowski, R. Avolio, G. Grancini, A. Petrozza, H. J. Snaith, *Nano Lett.* **2014**, *14*, 3247.

[30] L. Zhang, X. Liu, J. Su, J. Li, *J. Phys. Chem. C* **2016**, *120*, 23536.

[31] S. Bi, H. Wang, J. Zhou, S. You, Y. Zhang, X. Shi, Z. Tang, H. Zhou, *J. Mater. Chem. A* **2019**, *7*, 6840.

[32] M. A. Ruiz-Preciado, D. J. Kubicki, A. Hofstetter, L. McGovern, M. H. Futscher, A. Ummadisingu, R. Gershoni-Poranne, S. M. Zakeeruddin, B. Ehrler, L. Emsley, J. V. Milić, M. Grätzel, *J. Am. Chem. Soc.* **2020**, *142*, 1645.

[33] C. M. Wolff, L. Canil, C. Rehermann, N. Ngoc Linh, F. Zu, M. Ralaiarisoa, P. Caprioglio, L. Fiedler, M. Stolterfoht, S. Kogikoski, I. Bald, N. Koch, E. L. Unger, T. Dittrich, A. Abate, D. Neher, *ACS Nano* **2020**, *14*, 1445.

[34] S. Paek, C. Roldán-Carmona, K. T. Cho, M. Franckevičius, H. Kim, H. Kanda, N. Drigo, K. H. Lin, H. Pei, R. Gegevičius, H. J. Yun, H. Yang, P. A. Schouwink, C. Corminboeuf, A. M. Asiri, M. K. Nazeeruddin, *Adv. Sci.* **2020**, *7*, 2001014.

[35] J. Salunke, X. Guo, Z. Lin, J. R. Vale, N. R. Candeias, M. Nyman, S. Dahlström, R. Österbacka, A. Priimagi, J. Chang, P. Vivo, *ACS Appl. Energy Mater.* **2019**, *2*, 3021.

[36] E. Mosconi, J. M. Azpiroz, F. De Angelis, *Chem. Mater.* **2015**, *27*, 4885.

[37] D. Meggiolaro, E. Mosconi, A. H. Proppe, R. Quintero-Bermudez, S. O. Kelley, E. H. Sargent, F. De Angelis, *ACS Energy Lett.* **2019**, *4*, 2181.

[38] L. Canil, T. Cramer, B. Fraboni, D. Ricciarelli, D. Meggiolaro, A. Singh, M. Liu, M. Rusu, C. M. Wolff, N. Phung, Q. Wang, D. Neher, T. Unold, P. Vivo, A. Gagliardi, F. De Angelis, A. Abate, *Energy Environ. Sci.* **2021**, *14*, 1429.

[39] T. Yajima, Y. Hikita, M. Minohara, C. Bell, J. A. Mundy, L. F. Kourkoutis, D. A. Muller, H. Kumigashira, M. Oshima, H. Y. Hwang, *Nat. Commun.* **2015**, *6*, 6759.

[40] E. Zojer, T. C. Taucher, O. T. Hofmann, *Adv. Mater. Interfaces* **2019**, *6*, 1900581.

[41] A. Abate, R. Dehmel, A. Sepe, N. L. Nguyen, B. Roose, J. K. Hong, J. M. Hook, U. Steiner, C. Neto, *J. Mater. Chem. A* **2019**, *7*, 24445.

[42] R. Schölin, M. H. Karlsson, S. K. Eriksson, H. Siegbahn, E. M. J. Johansson, H. Rensmo, *J. Phys. Chem. C* **2012**, *116*, 26300.

[43] M. Ye, C. He, J. Iocozzia, X. Liu, X. Cui, X. Meng, M. Rager, X. Hong, X. Liu, Z. Lin, *J. Phys. D: Appl. Phys.* **2017**, *50*, 373002.

[44] T. Y. Chu, O. K. Song, *Appl. Phys. Lett.* **2007**, *90*, 073508.

[45] F. Zhang, Z. Yao, Y. Guo, Y. Li, J. Bergstrand, C. J. Brett, B. Cai, A. Hajian, Y. Guo, X. Yang, J. M. Gardner, J. Widengren, S. V. Roth, L. Kloo, L. Sun, *J. Am. Chem. Soc.* **2019**, *141*, 19700.

[46] Y. Wang, W. Chen, L. Wang, B. Tu, T. Chen, B. Liu, K. Yang, C. W. Koh, X. Zhang, H. Sun, G. Chen, X. Feng, H. Y. Woo, A. B. Djurišić, Z. He, X. Guo, *Adv. Mater.* **2019**, *31*, e1902781.

[47] T. Niu, W. Zhu, Y. Zhang, Q. Xue, X. Jiao, Z. Wang, Y. M. Xie, P. Li, R. Chen, F. Huang, Y. Li, H. L. Yip, Y. Cao, *Joule* **2021**, *5*, 249.

[48] S. G. Kim, T. H. Le, T. de Monfreid, F. Goubard, T. T. Bui, N. G. Park, *Adv. Mater.* **2021**, *33*, 2007431.

[49] Q. Fu, Z. Xu, X. Tang, T. Liu, X. Dong, X. Zhang, N. Zheng, Z. Xie, Y. Liu, *ACS Energy Lett.* **2021**, *6*, 1521.

[50] Q. Q. Ge, J. Y. Shao, J. Ding, L. Y. Deng, W. K. Zhou, Y. X. Chen, J. Y. Ma, L. J. Wan, J. Yao, J. S. Hu, Y. W. Zhong, *Angew. Chem., Int. Ed.* **2018**, *57*, 10959.

[51] M. Stolterfoht, M. Grischek, P. Caprioglio, C. M. Wolff, E. Gutierrez-Partida, F. Peña-Camargo, D. Rothhardt, S. Zhang, M. Raoufi, J. Wolansky, M. Abdi-Jalebi, S. D. Stranks, S. Albrecht, T. Kirchartz, D. Neher, *Adv. Mater.* **2020**, *32*, 2000080.

[52] M. Stolterfoht, P. Caprioglio, C. M. Wolff, J. A. Márquez, J. Nordmann, S. Zhang, D. Rothhardt, U. Hörmann, Y. Amir, A. Redinger, L. Kegelmann, F. Zu, S. Albrecht, N. Koch, T. Kirchartz, M. Saliba, T. Unold, D. Neher, *Energy Environ. Sci.* **2019**, *12*, 2778.

[53] S. A. L. Weber, I. M. Hermes, S. H. Turren-Cruz, C. Gort, V. W. Bergmann, L. Gilson, A. Hagfeldt, M. Graetzel, W. Tress, R. Berger, *Energy Environ. Sci.* **2018**, *11*, 2404.

[54] H. J. Snaith, A. Abate, J. M. Ball, G. E. Eperon, T. Leijtens, N. K. Noel, S. D. Stranks, J. T. W. Wang, K. Wojciechowski, W. Zhang, *J. Phys. Chem. Lett.* **2014**, *5*, 1511.

[55] W. Tress, *J. Phys. Chem. Lett.* **2017**, *8*, 3106.

[56] G. Richardson, S. E. J. O'Kane, R. G. Niemann, T. A. Peltola, J. M. Foster, P. J. Cameron, A. B. Walker, *Energy Environ. Sci.* **2016**, *9*, 1476.

[57] N. E. Courtier, G. Richardson, J. M. Foster, *Energy Environ. Sci.* **2019**, *12*, 396.

[58] R. Roesch, T. Faber, E. Von Hauff, T. M. Brown, M. Lira-Cantu, H. Hoppe, *Adv. Energy Mater.* **2015**, *5*, 1501407.

[59] M. V. Khenkin, E. A. Katz, A. Abate, G. Bardizza, J. J. Berry, C. Brabec, F. Brunetti, V. Bulović, Q. Burlingame, A. Di Carlo, M. Matheron, M. Mcgehee, R. Meitzner, M. K. Nazeeruddin, *Nat. Energy* **2020**, *5*, 35.

[60] K. Domanski, E. A. Alharbi, A. Hagfeldt, M. Grätzel, W. Tress, *Nat. Energy* **2018**, *3*, 61.

[61] Y. Zhao, W. Zhou, Z. Han, D. Yu, Q. Zhao, *Phys. Chem. Chem. Phys.* **2021**, *23*, 94.

[62] K. Domanski, B. Roose, T. Matsui, M. Saliba, S. H. Turren-Cruz, J. P. Correa-Baena, C. R. Carmona, G. Richardson, J. M. Foster, F. De Angelis, J. M. Ball, A. Petrozza, N. Mine, M. K. Nazeeruddin, W. Tress, M. Grätzel, U. Steiner, A. Hagfeldt, A. Abate, *Energy Environ. Sci.* **2017**, *10*, 604.